Journal of Molecular Structure 1155 (2018) 424–433

Contents lists available at ScienceDirect

Journal of Molecular Structure

journal homepage: http://www.elsevier.com/locate/molstruc

A detailed study of intermolecular interactions, electronic and vibrational properties of the metal complex bis(uracilato)diammine copper(ii) dihydrate

M. Gramajo Feijoo [a, b], M.P. Fernández-Liencres [c], D.M. Gil [a, b, 1], M.I. Gómez [d], A. Ben Altabef [a, b, 1], A. Navarro [c], M.E. Tuttolomondo [a, b, *]

[a] Instituto de Química Física, Facultad de Bioquímica, Química y Farmacia, Universidad Nacional de Tucumán, San Lorenzo 456, T4000CAN, Tucumán, Argentina
[b] Instituto de Química del Noroeste Argentino, INQUINOA, CONICET, Tucumán, Argentina
[c] Department of Physical and Analytical Chemistry, Faculty of Experimental Sciences, Universidad de Jaén, Campus Las Lagunillas, 23071, Jaén, Spain
[d] Instituto de Química Inorgánica, Facultad de Bioquímica, Química y Farmacia, Universidad Nacional de Tucumán, Ayacucho 491, T4000CAN, Tucumán, Argentina

ARTICLE INFO

Article history:
Received 20 July 2017
Received in revised form
4 November 2017
Accepted 8 November 2017
Available online 8 November 2017

Keywords:
Cu(uracilato-N^1)$_2$ (NH_3)$_2$] $2H_2O$ complex
Synthesis
FTIR
Raman
DFT

ABSTRACT

Density Functional Theory (DFT) calculations were performed with the aim of investigating the vibrational, electronic and structural properties of [Cu(uracilato-N^1)$_2$ (NH_3)$_2$]·$2H_2O$ complex. The IR and Raman spectra were recorded leading to a complete analysis of the normal modes of vibration of the metal complex.

A careful study of the intermolecular interactions observed in solid state was performed by using the Hirshfeld surface analysis and their associated 2D fingerprint plots. The results indicated that the crystal packing is stabilized by N–H···O hydrogen bonds and π-stacking interactions. In addition, C–H···π interactions were also observed.

Time-dependent density functional theory (TD-DFT) calculations revealed that all the low-lying electronic states correspond to a mixture of intraligand charge transfer (ILCT) and ligand-to-metal charge transfer (LMCT) transitions.

Finally, Natural Bond Orbital (NBO) and Atoms in Molecules (AIM) analysis were performed to shed light on the intermolecular interactions in the coordination sphere.

1. Introduction

For more than fifty years, the interactions of metal ions with nucleic acids and their constituents have been studied due to the importance of metal ions in biologically important processes. Over the years, a large number of data involving thermodynamic and kinetic properties, metal binding sites and normal modes of vibration have been reported in literature [1–9]. Several metal ions, such as Zn^{2+}, Ca^{2+}, Cu^{2+}, Mn^{2+} and Mg^{2+}, are commonly found in living organisms, acting as structure promoters or playing important roles in enzymatic activity. A comprehensive knowledge of metal binding modes is crucial for understanding the effects of metal ions on the nucleobase or the nucleic acid and for its translation into biology [9]. Copper (II) complexes using uracil as ligand are of great pharmacological interest because they show a wide spectrum of biological properties, including anti-inflammatory, anti-ulcer, anti-convulsant and even anti-tumoral activity [4–8]. The presence of the uracil ring favours that the resultant compounds have a structure analogous to other species found in biological systems, what is useful to their potential pharmacologic applications [9].

This work is focussed on the metal complex [Cu(uracilato-N^1)$_2$(NH_3)$_2$]·$2H_2O$ whose synthesis and structural characterization were reported by Terrón and co-workers [6]. The crystal structure was solved by single-crystal X-ray diffraction techniques although a detailed analysis of the intermolecular interactions in solid state

* Corresponding author. Instituto de Química Física, Facultad de Bioquímica, Química y Farmacia, Universidad Nacional de Tucumán, San Lorenzo 456, T4000CAN, Tucumán, Argentina.
E-mail address: metuttolomondo@fbqf.unt.edu.ar (M.E. Tuttolomondo).
[1] Members of the Research Career of CONICET.

https://doi.org/10.1016/j.molstruc.2017.11.030
0022-2860/

was not carried out.

In the present contribution, the complex [Cu(uracilato-N^1)$_2$(NH_3)$_2$]·2H_2O has been synthesized and characterized by different spectroscopic techniques such as UV–Vis, Infrared and Raman spectroscopies. In addition, the thermal behavior was studied by Thermogravimetric (TG) and Differential Thermal Analysis (DTA). One of the goal of this work has been to study the UV–visible spectrum in the solid state in order to assign the multi configurational electronic transitions and the d–d transitions for the Cu(II) complex. In addition, the stability of the complex in terms of hyper-conjugative and charge transfer interactions have been studied through the Second Order Perturbation Theory of the Fox Matrix by using the NBO analysis. The AIM theory [10] has been used to analyze the topology of all the optimized structures. Furthermore, Hirshfeld surface analyses have been performed in order to understand the nature of packing of molecules in the crystal structure, highlighting the contribution of significant interactions between molecules that are responsible of the molecular arrangement in the solid.

2. Experimental

2.1. Synthesis

The preparation of the bis(uracilato)diammine copper (II) complex was performed by the technique previously reported by Terrón et al. [6]. Uracil (2 mmol) was dissolved in aqueous concentrated ammonia (10 mL) at room temperature. When the ligand was completely dissolved, an equimolar amount of $CuSO_4·5H_2O$ (1 mmol) was added dropwise with continuous stirring. The mixture was refluxed with stirring during 30 min and then the intense blue solution was left to evaporate slowly. After several days, crystals of the corresponding product appeared.

2.2. Characterization techniques

FTIR measurements were carried out in a Perkin Elmer GX spectrophotometer provided with a DTGS detector constantly purged with dry air. The infrared spectra of solid samples were recorded at room temperature in KBr pellets with a resolution of 1 cm^{-1} in the 4000-400 cm^{-1} range. A total of 64 scans were done in each measurement and the spectra were analyzed by using the OMNIC v.7.2 mathematical software provided by the manufacturer. The standard deviation of the wavenumber shift calculated from this pool of data was about ±1.5 cm^{-1} in all the conditions assayed. The Fourier Self Deconvolution algorithm was applied to define the contours of overlapping bands.

The dispersion Raman spectra of solid samples were recorded using a confocal Thermo Scientific-DXR Raman Microscope equipped with a high resolution motorized platen, a set of Olympus optical objectives, a lighting module bright field/dark field trinocular viewer, an Olympus camera of 2048 pixels with CCD detector, cooled by Peltier module and an OMNIC Atlμs Mapping software of advanced features. The confocal system is real, with opening/hole matched with the point of symmetry of the excitation laser. The resolution is 2 μm in depth profiles. The standard spatial resolution was better than 1 μm. The samples were placed on gold-coated sample slides. In order to achieve a sufficient signal-to-noise ratio, 100 acquisitions with exposure time of 5 s were accumulated for all samples. The laser power was used at 10 mW and the laser wavelength was 532 nm (5 cm^{-1} spectral resolution). All spectroscopic experiments were carried out at room temperature. The spectra were analyzed using the OMNIC™ program for Dispersive Raman.

Thermogravimetric (TG) and Differential Thermal Analysis (DTA) measurements were performed with Shimadzu TG-50 and DTA-50 equipments in the temperature range of 25–800 °C, at heating rate 5°C/min under flowing air.

2.3. Theoretical methods

Full geometry optimization and vibrational frequency calculations were performed in the isolated molecule using the B3LYP hybrid functional in combination with the LanL2DZ effective core potentials basis set [11a-c] for the Cu atom and the 6–311++G (d,p) basis set [12,13] for C, N, O and H atoms. The complex was treated as an open-shell system using spin unrestricted DFT wavefunctions (UB3LYP). In addition, Natural Bond Orbital (NBO) calculations were performed at the B3LYP/LanL2DZ level of theory using the NBO 3.1 program [14–16] implemented in the GAUSSIAN 09 program package [17]. AIM calculations were performed with the help of AIM2000 program [18]. The atomic displacements given by the Gaussian program for each vibrational mode were used to understand qualitatively the nature of the molecular vibrations and, for that purpose, the corresponding data were represented graphically using the GaussView program [19]. Based on the optimized geometries in the ground state of the studied complex, TD-DFT calculations were performed at the same level of theory (UB3LYP) to calculate the vertical electronic transitions associated with the absorption spectrum [20,21].

2.4. Hirshfeld surface calculations

Hirshfeld surfaces and their associated bidimensional fingerprint plots [22–25] were drawn using the CrystalExplorer3.1 program [26]. The crystallographic information file (.cif) of the structure was imported into CrystalExplorer and a high resolution Hirshfeld surface was mapped with the functions d_{norm}, *Shape Index* and *Curvedness*. Graphical plots of the molecular Hirshfeld surfaces mapped with d_{norm} function show regions with red, blue and white colors where red highlights indicate shorter contacts, white is used for contacts around the vdW separation and blue indicate longer contacts.

Curvedness is a function of the root-mean-square curvature of the surface. Low values of curvedness are associated with essentially plat areas of the surface, while areas of sharp curvature possess a high curvedness and tend to divide the surface into patches associated with contacts between neighboring molecules. Shape index is a measure of "which shape" and it can be sensitive to very subtle changes in surface shape, particularly in areas where the total curvature (or the curvedness) is very low. Red triangles on Shape Index indicate concave regions and it is an indicative of $\pi\cdots\pi$ stacking interactions. The 2D fingerprint plots have been used to evaluate molecular shapes and give us a percentage of all main intermolecular interactions. This analysis is very useful in the exploration of the packing modes and intermolecular interactions. The 3D d_{norm} surfaces are mapped over a fix color scale of −0.425 au (red) to 1.324 au (blue), the *shape index* in the color range −1.0 au (concave) to 1.0 au (convex), and *curvedness* in the range of −4.0 au (flat) to 0.1 au (singular). The 2D Fingerprint plots were drawn by using the standard 0.6–2.4 Å and including reciprocal contacts.

3. Results and discussion

3.1. Structural properties

DFT calculations were carried out for the complex in gas phase in order to optimize the ground state structure and to obtain the vibrational frequencies. The optimized molecular structure

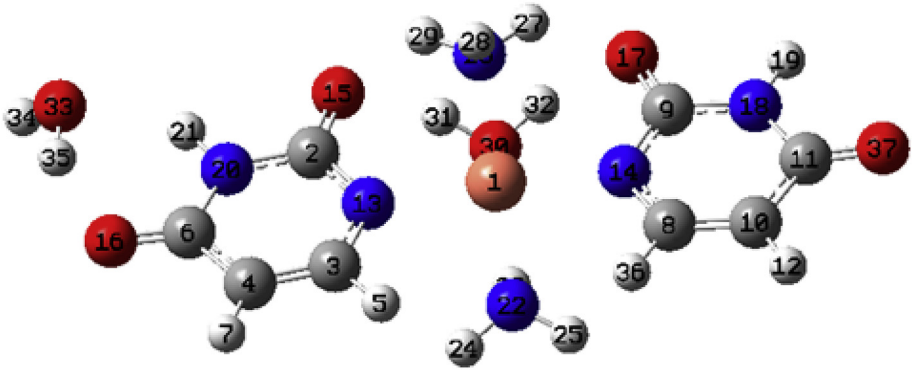

Fig. 1. Optimized molecular structure and atom numberings for bis(uracilato)diammine Cu (II) complex.

calculated at the B3LYP level is shown in Fig. 1 and the main geometrical parameters are listed in Table 1. The experimental XRD data previously reported [6] have been used for comparison (See Table 1). The root mean square deviation (RMS) was calculated for bond distances and bond angles. In general, a good agreement has been observed between the calculated and experimental geometrical parameters in terms of the RMS values for bond distances ~0.12 Å and for bond angles ~0.99° (Table S1).

As can be seen in Table 1, the M-N(ligand) bond distances are slightly overestimated by the calculations. Thus, the experimental values of the Cu–N(13) and Cu–N(14) bond lengths are 1.985 and 1.999 Å, and they are predicted at 2.033 and 2.034 Å respectively. Also, the bond lengths associated to the ammine group, Cu–N(22) and Cu-(N26), take an experimental value of 2.013 Å and they are estimated at 2.100 and 2.068 Å. In contrast, the Cu–O bond distance is theoretically underestimated (see Table 1). As a conclusion, the optimized structure of the $[Cu(uracilato\text{-}N^1)_2(NH_3)_2]\cdot 2H_2O$ confirms the distorted square planar geometry proposed by Terrón and co-workers [6].

These results are also in accordance with the experimental data obtained by the IR, Raman, UV–Vis and TG-DTA techniques (see below) indicating that the Cu(II) ion is tetra-coordinated through two nitrogen atoms of each uracil ligand as well as two nitrogen atoms of the NH_3 groups. The water molecules have zeolitic character and they interact with amino groups and uracil ligands through intramolecular hydrogen bonding interactions (see Table S2).

Table 1
Selected experimental and calculated geometric parameters for bis(uracilate) diammine copper(II) complex.

Parameters	Experimental Ref. [6]	Calculated
Bond distances (Å)		
Cu–N(13)	1.985	2.033
Cu–N(14)	1.999	2.034
Cu–N(22)	2.013	2.100
Cu–N(26)	2.013	2.068
Cu–-O(30)	2.890	2.380
N(26)–O(15)	2.522	2.114
N(26)–O(17)	2.669	2.117
N(22)–H–-O(30)	2.687	2.245
O(30)–H–-O(15)	2.150	1.916
O(30)–H–-O(17)	2.359	1.926
Angles (°)		
N(14)–Cu–N(13)	168.1	166.0
N(14)–Cu–N(22)	91.3	89.9
N(14)–Cu–N(26)	90.1	90.8
N(22)–Cu–N(26)	166.8	172.0

3.2. Thermal behavior

The TG and DTA curves for the thermal decomposition of the complex $[Cu(uracilato\text{-}N^1)_2\ (NH_3)_2]\ \cdot 2H_2O$ in air are presented in Fig. 2. The complex decomposes in steps unresolved. The total mass loss at around 300 °C is 78.2%. It is in accordance with the theoretical value (77.6%) calculated for the formation of CuO from the complex.

The DTA curve shows two exothermic peaks located at 229 and 255 °C. The first one is attributed to the water elimination by a slow process and the second one is associated to the decomposition of the complex which occurs at low temperature through a quick stage.

The decomposition process in an oxidative atmosphere can be represented by the following equations:

$$[Cu(Uracilato\text{-}N^1)_2(NH_3)_2]\cdot 2H_2O_{(s)} \rightarrow [Cu(Uracilato\text{-}N^1)_2(NH_3)_2]_{(s)} + 2H_2O_{(g)}$$

$$[Cu(Uracilato\text{-}N^1)_2(NH_3)_2]_{(s)} + O_{2(g)} \rightarrow CuO_{(s)} + \text{volatile products}$$

3.3. Electronic properties

In order to investigate the electronic transitions from the ground state to the excited states, Time-dependent density functional theory (TD-DFT) calculations have been performed at the UB3LYP level. The calculated vertical transitions have been assigned to the

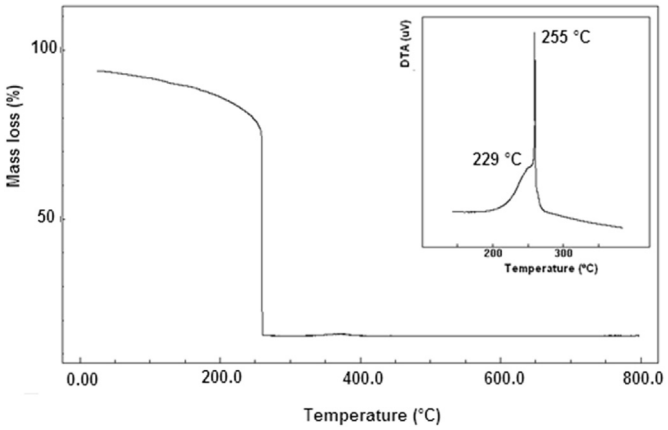

Fig. 2. TG curve for the thermal decomposition of $[Cu(Uracilato\text{-}N^1)_2(NH_3)_2]\cdot 2H_2O$ at 5°/min in air. Inset: DTA curve between 150 and 350 °C.

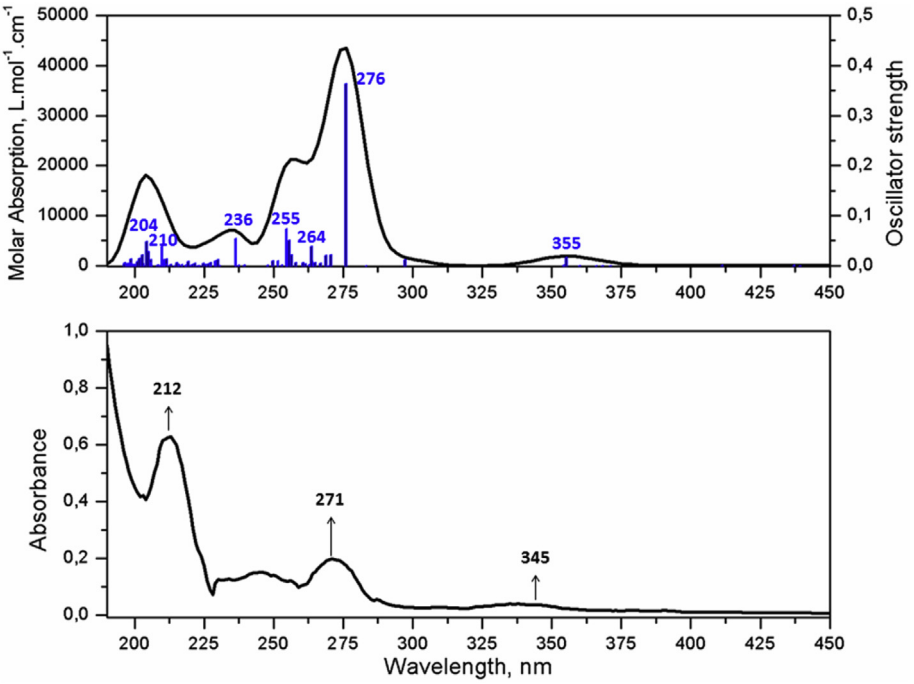

Fig. 3. Experimental (down) and calculated (up) UV–Vis absorption spectra for [Cu(uracilato-N^1)$_2$ (NH_3)$_2$] ·2H_2O complex at the TD-DFT/B3LYP level of theory.

experimental bands taken into account the predicted energy value and the oscillator strength. The theoretical absorption spectrum for the [Cu(uracilato-N^1)$_2$ (NH_3)$_2$]·2H_2O complex together with the experimental UV–Vis spectrum are shown in Fig. 3 for comparison. The band assignments along with the energies and the oscillator strengths are collected in Table 2. In the description of the electronic transitions, only the main components of the molecular orbitals are considered. The α and β-spin molecular orbitals, especially those related to the high energy electronic transitions, are presented in Fig. 4. The orbitals with *d* character are intermixed with the ligand orbitals.

TD-DFT results reveal that the $S_0 \rightarrow S_1$ transition corresponds to

Table 2
Experimental UV–Vis wavelength and calculated vertical transitions, oscillator strengths (*f*) and assignments for the [Cu(uracilato-N^1)$_2$ (NH_3)$_2$]·2H_2O complex.

Excitation	Exp.	Calculated				
	λ(nm)	E(eV)	λ(nm)	f	Transition configuration (%)	Assignment[a]
1		1.57	787	0.0001	HOMO (β) →LUMO (β) (0.60)	LMCT
					HOMO-1 (β) → LUMO (β) (0.21)	LMCT
2		1.72	721	0.0004	HOMO-9(β) → LUMO (β) (0.35)	LMCT
					HOMO-1 (β) → LUMO (β) (0.29)	LMCT
3		1.97	630	0.0008	HOMO-1 (β) → LUMO (β) (0.41)	LMCT
					HOMO-9 (β) → LUMO (β) (0.22)	LMCT
					HOMO (β) → LUMO (β) (0.19)	LMCT
13	345	3.49	355	0.0167	HOMO-6 (β) → LUMO (β) (0.44)	LMCT
					HOMO-7 (β) → LUMO (β) (0.43)	LMCT
17	271	4.49	276	0.3634	HOMO-10 (β) → LUMO (β) (50)	LMCT
					HOMO-17 (β) → LUMO (β) (16)	d–d/LMCT
24		4.70	264	0.0379	HOMO-11 (β) → LUMO (β)	LMCT
30		4.85	256	0.0508	HOMO-1 (α) → LUMO (α) (17)	ILCT
					HOMO (α) → LUMO+2 (α) (13)	ILCT
					HOMO-1 (α) → LUMO+2 (α) (19)	ILCT
					HOMO-1 (β) → LUMO+2 (β) (20)	ILCT
					HOMO-1 (β) → LUMO+3 (β) (16)	LMCT/ILCT
31		4.87	255	0.0736	HOMO (α) → LUMO+1 (α) (51)	ILCT
					HOMO (β) → LUMO+2 (β) (32)	ILCT
38		5.24	236	0.0537	HOMO-13 (β) → LUMO (β) (49)	LMCT
					HOMO-15 (β) → LUMO (β) (34)	d–d/LMCT
68	212	5.91	210	0.0389	HOMO-6 (α) → LUMO (α) (11)	ILCT
					HOMO-5 (α) → LUMO+1 (α) (18)	ILCT
					HOMO-5 (β) → LUMO+2 (β) (12)	ILCT
					HOMO-4 (β) → LUMO+3 (β) (19)	ILCT/LMCT
76		6.07	204	0.0478	HOMO-5 (α) → LUMO+1 (α) (13)	ILCT
					HOMO-5 (β) → LUMO+2 (β) (26)	ILCT
					HOMO-4 (β) → LUMO+3 (β) (14)	ILCT/LMCT

[a] ILCT= Intraligand charge transfer; LMCT = ligand to metal charge transfer.

a HOMO-LUMO excitation. The energy of the α-HOMO (−6.72 eV) is similar to that of the β-HOMO (−6.68 eV) while the energy of the β-LUMO (−3.93 eV) is less than that of the α-LUMO (−1.48 eV) because the Cu^{2+} orbitals overlap with the ligand orbitals in the β-LUMO. These results evidence that the HOMO-LUMO energy difference of the α-MOs gap is larger (ΔE = 5.24 eV) compared to the corresponding value of β-MOs (ΔE = 2.75 eV), and the lowest excitation occurs between β-HOMO and β-LUMO.

The experimental spectrum in solid state shows a strong band in the region 200–220 nm (λ_{max} = 212 nm) and other band in the region 265–290 nm (λ_{max} = 271 nm). The first band is calculated in gas phase at 204–210 nm which is mainly assigned to n→π* transitions because of the intraligand charge transfer (ILCT) in uracil. The second band is calculated at 276 nm which is related to the ligand-to-metal charge transfer (LMCT). The additional less intense peak at 345 nm can be attributed to a LMCT transition. Despite the fact that the region 225–260 nm is not resolved in the experimental spectrum, the calculations have revealed an absorption band at 255–256 nm which is mainly a π→π* transition due to the intraligand charge transfer (ILCT) in uracil and with contributions of the NH_3 ligands; another band is calculated at 236 nm which is a LMCT transition.

From our calculations, we have also predicted low energy weak absorption bands at 787, 721 and 630 nm with very small oscillator strengths which are too weak to be observed in the experimental spectrum of the complex. From the analysis of the molecular orbitals, we have suggested that these transitions are related to both DMSO-d_6 and LMCT transitions.

3.4. Hirshfeld surface analysis

Hirshfeld surface analyses have been performed in order to understand the nature of packing of molecules in the crystal structure, highlighting the contribution of significant interactions between molecules that are responsible of the molecular arrangement in the solid. In accordance with the crystal structure reported by Terrón et al. [6], the copper complex $[Cu(Uracilato\text{-}N^1)_2(NH_3)_2]\cdot 2H_2O$ crystallizes in the orthorhombic crystal system, space group *Pnma* and with four molecules per unit cell. Intramolecular N–H···O hydrogen bonds are observed and these interactions are produced by the contact of the hydrogen of the ammonia group and the oxygen of the water molecules and the carbonyl group. The geometrical parameters of the intramolecular and intermolecular interactions are shown in Table S2. In the crystal packing of the complex, the molecules are linked via classical N–H···O hydrogen bonds generating $R_2^2(8)$ graf-set ring motifs (see Fig. S1). The supramolecular structure of the complex also includes the existence of intermolecular C–H···π interactions, as shown in Fig. 5A.

The structure of the complex is also stabilized by intermolecular π···π interactions with off-set facial arrangement, as can be seen in Fig. 5B. The long values of centroid to centroid distance indicate weak π-stacking interactions in the complex (See Fig. 5B).

For a complete understanding of the combined participation of hydrogen bonds and π-stacking interactions in the complex, the Hirshfeld surfaces and their associated 2D fingerprint plots were generated. The Hirshfeld surfaces of the complex mapped over a d_{norm} function are shown in Fig. 6. The two larger red regions on the bottom right and upper left on the d_{norm} surfaces (labeled as **1**) are

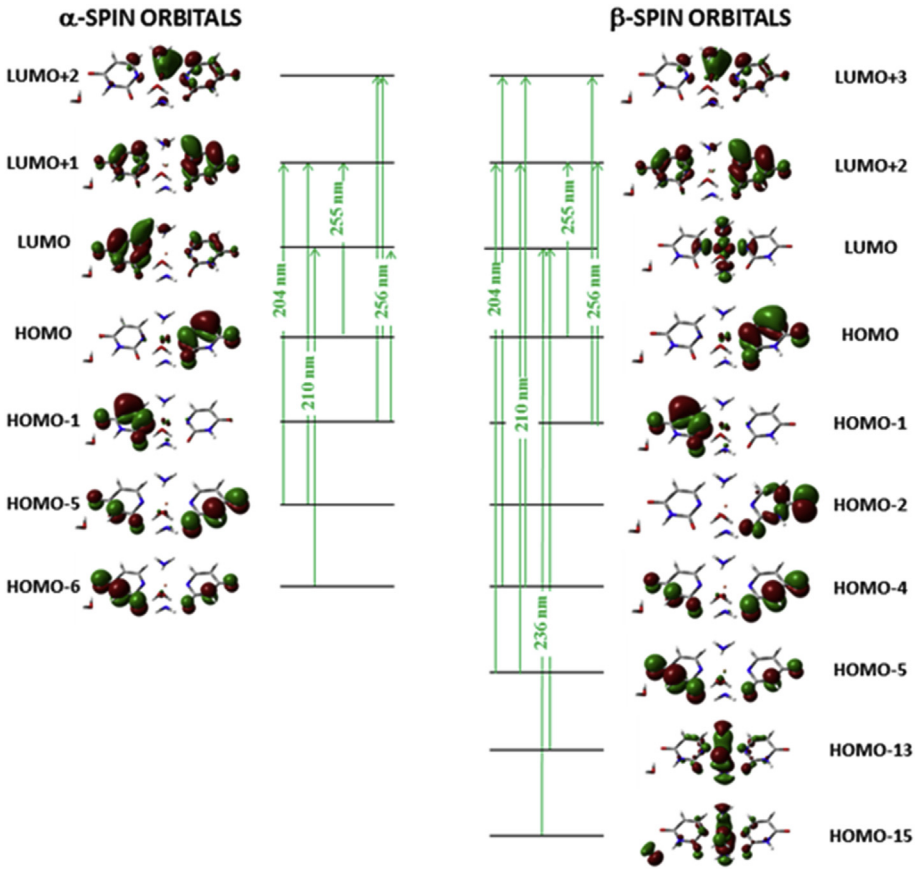

Fig. 4. Diagram showing high energy electronic transitions in $[Cu(uracilato\text{-}N^1)_2(NH_3)_2]\cdot 2H_2O$ (orbital contour value = 0.035).

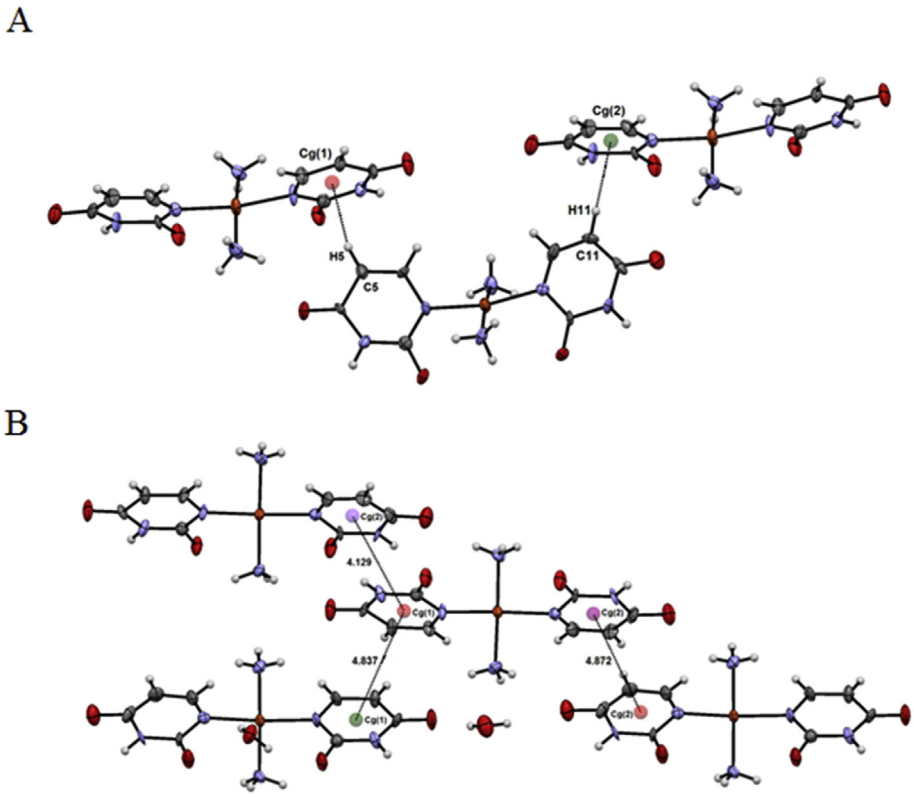

Fig. 5. (A) Crystal packing of the complex $[Cu(Uracilato\text{-}N^1)_2(NH_3)_2]\cdot 2H_2O$ showing the π-stacking interactions. The Cg(1)···H5 and Cg(2)···H11 contacts are shown in dashed lines. Symmetry codes: (a) ½+x, ½-y, -z; (b) ½+x, ½-y, 1-z. **(B)** A view of the π-stacking interactions showing Cg(1)···Cg(1), Cg(2)···Cg(1) and Cg(2)···Cg(2) contacts.

attributed to N–H···O type hydrogen bonding interactions. These interactions are between the N–H group of the uracil ring and the oxygen from the carbonyl group. These interactions are discussed previously. The red areas marked as **2** and **3** are associated with N–H···O interactions between the NH_3 group and the non-coordinated water molecules and between the oxygen atom from the carbonyl group. The red spots labeled as **4** and **5** correspond to C–H···π and O–H···O interactions, respectively.

In order to evaluate π-stacking interactions in the solid, a close examination of the Hirshfeld surfaces mapped over Shape Index and Curvedness (see Fig. 6) was performed. These interactions are evident in the Hirshfeld surface as a large flat region across the molecule, which is most clearly visible on the Curvedness surface. The pattern of red and blue triangles on the same region of the Shape Index surface is another clear characteristic of π···π interactions. The pattern of alternating red and blue triangles with suitable symmetry is indicative of offset π-stacking interactions characteristic of layers and this type of stacking is evident in this compound. Generally, the π···π interactions are not visible in the d_{norm} map because the corresponding C···C distances between the uracil rings are longer than sum of vdW radii, as can be seen in the crystallographic data.

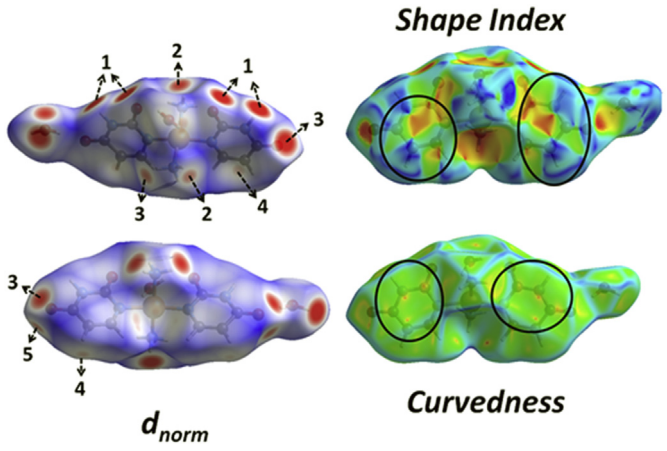

Fig. 6. Hirshfeld surfaces mapped with d_{norm}, Shape Index and Curvedness for the metal complex. The complex is shown in two orientations in the d_{norm} plot. The number arrows are discussed in the text.

The 2D Fingerprint plots are used for identification and separation of intermolecular interactions and relative contribution of these interactions could be obtained from the area of the surfaces. The 2D fingerprint plots of the complex, displayed by the standard view, are shown in Fig. 7.

For the structure of the complex, the sharp pair of spikes labeled as 1 are attributed to O···H interactions. They have the lowest value of $(d_e + d_i)$ sum of 1.8 Å. The contacts labeled as 2 correspond to the very close H···H contacts. These contacts generally are not visible on the Hirshfeld surface because their distances are longer than the sum of vdW radii. A pair of broad wings (column 2) labeled 3 around $(d_e + d_i)$ of 2.65 Å is evidence of C···H contacts. The point labeled 4, with $d_e = d_i \approx 1.8$ Å are characteristic of π···π interactions.

The intermolecular O···H contacts have the major contribution to the crystal packing (43.5%) and the H···H contacts comprise 33.4% of total Hirshfeld surface area of the complex. Other types of intermolecular contacts with the most important percentages occur such as C···H (13.1%), N···H (3.3%), C···N (1.5%) and C···C (1.2%).

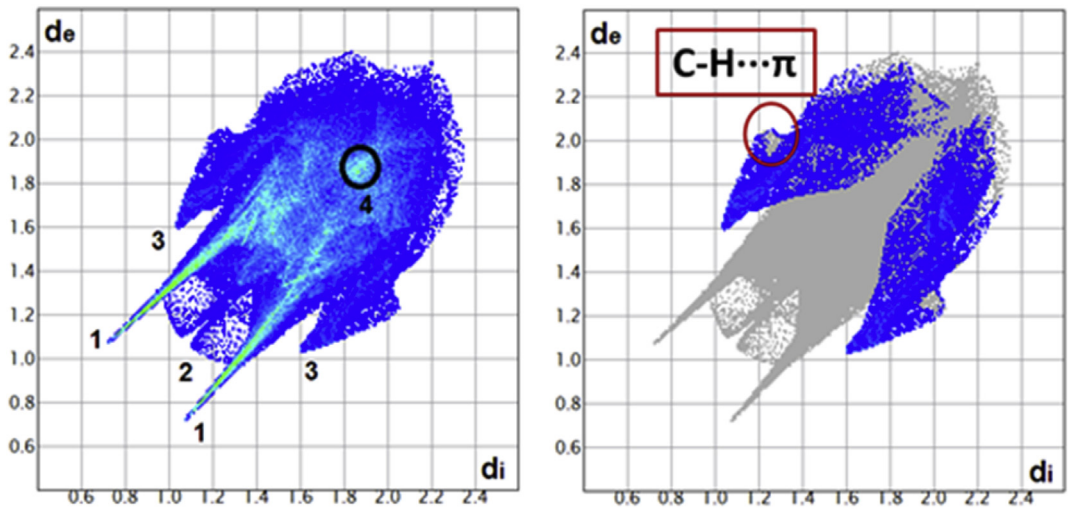

Fig. 7. 2D Fingerprint plots for Cu(Uracilato-N^1)$_2$(NH_3)$_2$]·2H_2O showing: (1) O···H, (2) H···H, (3) C···H, (4) C···C intermolecular contacts.

3.5. Vibrational properties

The bis(uracilato)diammine Copper (II) complex presents 110 normal modes of vibration that are active in both the IR and Raman spectra. Representative IR and Raman spectra of the complex in solid state appear in Fig. 8 and the vibrational wavenumbers of the observed spectral features appear in Table S3. A complete assignment of the IR and Raman wavenumbers of the metal complex in solid state was made, with some corrections in the previous assignment of the uracil ligand. The experimental (solid state) and calculated (isolated) IR spectra of the metal complex are shown in Fig. 9 where some assignments are also included.

The OH stretching modes of the water molecules are strongly mixed with the stretching modes of the NH_3 ligands. These bands are clearly observed in the calculated spectrum, whereas in the experimental one these bands appear as a broad band at 3452 cm^{-1} (See Fig. 9). The bands observed between 3100 and 2900 $cm^{-1}$are assigned to the C–H stretching modes of the uracil ligand. These bands are slightly shifted to lower frequencies taking into account the previous assignments of the uracil ligand [27]. These results are in agreement with the coordination of the uracil ligand to the metal center.

The calculated and experimental IR spectra between 1700 and 400 cm^{-1} are presented in Fig. 10. The broad band between 1700 and 1500 cm^{-1} is attributed to a mixture of C = O stretching mode and the bending modes of water molecules. This band was deconvoluted and the involved modes were assigned by comparison with the calculated spectrum.

The observed bands at 1658 and 1642 cm^{-1} are assigned to C = O stretching modes, while the bands at 1627 and 1608 cm^{-1} are assigned to δ(HOH) and δ(NH) (uracil) bending modes, respectively. The lower value of the frequency observed for the C=O stretching mode is consistent with the O–H···O(keto) hydrogen bonding interaction observed in the solid state (See section 3.4). The NH_3 asymmetric and symmetric bending modes are clearly observed at 1509 and 1456 cm^{-1}, respectively.

The solid state Raman spectrum of the complex is shown in Fig. 11. The band located at 1640 cm^{-1} is assigned to the C=C stretching mode of the uracil ligand. This band is clearly observed at 1652 cm^{-1} in the Raman spectra of the free uracil [28].

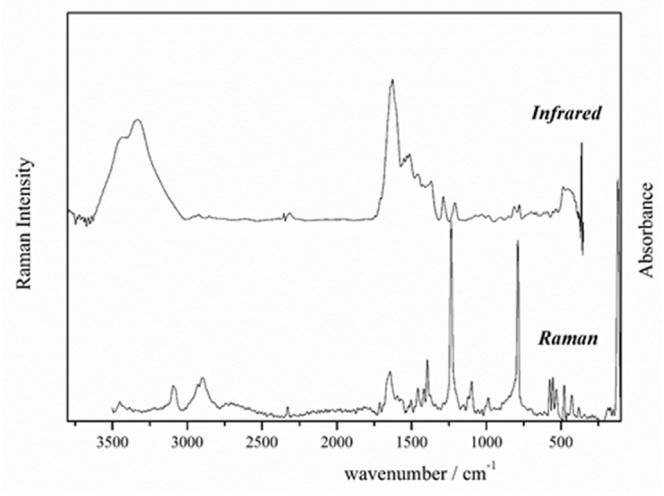

Fig. 8. IR and Raman spectra of the solid phase for bis(uracilato)diammine Copper (II) complex.

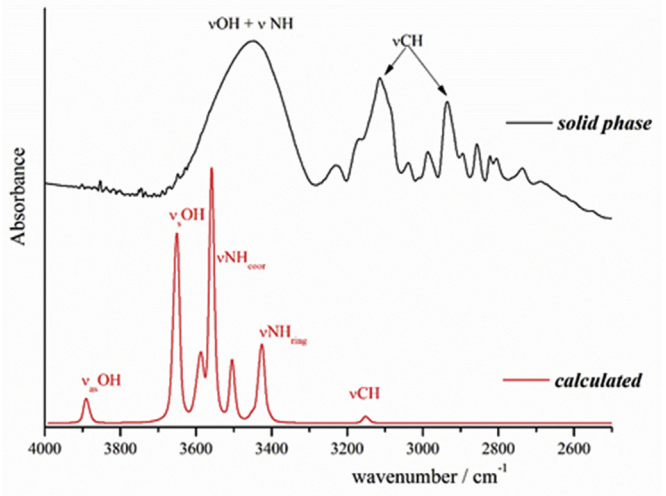

Fig. 9. FTIR spectra (between 4000 and 2600 cm^{-1}) of the experimental (solid phase, black) and calculated (isolated, red) for bis(uracilato)diammine Copper (II) complex. (For interpretation of the references to colour in this figure legend, the reader is referred to the web version of this article.)

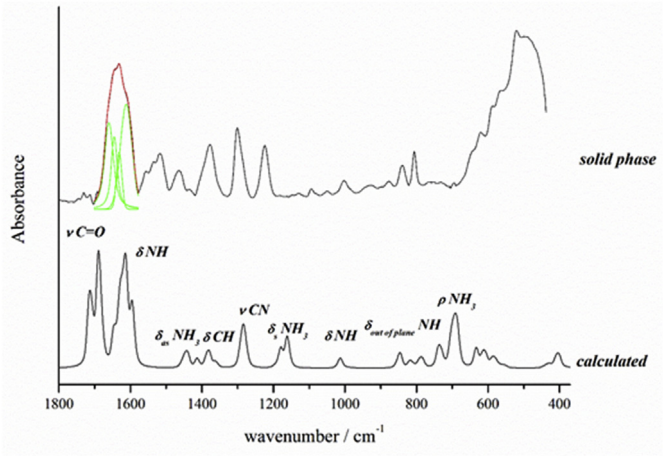

Fig. 10. FTIR spectra of the experimental and calculated for bis(uracilato)diammine Cu (II) complex. The black line represents the contours of the acquired spectra, and the green and red lines represent our estimates of the position and relative intensities of the component bands after their deconvolution and fitting, respectively. (For interpretation of the references to colour in this figure legend, the reader is referred to the web version of this article.)

The assignments of the vibrations related to the coordination sphere are difficult to identify. Two bands at 382 and 312 cm^{-1} appear in the Raman spectrum of the solid, which are assigned to the Cu–NH_3 stretching mode, while they are calculated at 378 and 314 cm^{-1}. The calculated Raman spectrum shows a very low intensity band at 253 cm^{-1} due to the Cu-N_{uracil} stretching mode, which could be assigned in the Raman spectrum of the solid at 252 cm^{-1} [5].

3.6. Topological analysis

To rationalize the coordination sphere of the complex, we used the Bader's Atoms In Molecules (AIM) quantum theory [10]. This theory has been repeatedly shown to be of aid in the characterization of bonds through a topological analysis of the electronic charge density and its Laplacian at the bond critical point (BCP). Within the AIM theory, the nature of the bonding interaction can be determined through an analysis of the properties of charge density $\rho(r)$ and its Laplacian $\nabla^2\rho(r)$ at the BCP, and through the properties

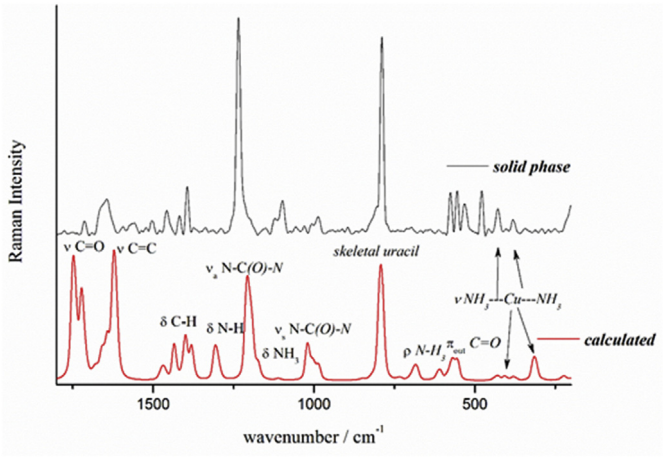

Fig. 11. Experimental and calculated Raman spectra of the bis(uracilato)diammine Cu (II) complex.

of the atoms, which are obtained by integrating the charge density over the atomic basin.

Several properties evaluated at the BCP make up powerful tools to classify a given chemical structure [10,29]. Briefly, two negative eigenvalues of the Hessian matrix (λ_1 and λ_2, respectively) measure the degree of contraction of $\rho(r)$ at a normal direction to the bond towards the BCP, while a positive eigenvalue (i.e., λ_3) gives a quantitative indication of the contraction degree parallel to the bond and from the BCP towards each of the neighboring nuclei.

The density contour map for the complex is shown in Fig. 12 **(a)** which reveals a slightly distorted square structure. The contour map of $\nabla^2\rho(r)$ for the complex is shown in Fig. 12 **(b)**. The solid lines correspond to negative values of $\nabla^2\rho(r)$ indicating the areas of concentration of the electron density, whereas the dotted lines indicate areas of depression of the electron density with positive values of $\nabla^2\rho(r)$.

The interactions that contribute to the stability of the studied compound can be divided into two groups. The main group consists of metal–ligand (Cu–N) interactions, and the second one corresponds to hydrogen bonding interactions, both ligand-ligand and water molecule-ligand [30].

The values of the electron densities calculated for the Cu–N(uracil) bonds are slightly higher than those calculated for the Cu–N(ammonia) indicating that the latter interactions are somewhat weaker than the former (see Table 3).

The positive values of $\nabla^2\rho(r)$ for the metal–ligand bonds indicate the electrostatic nature of these interactions. When the positive eigenvalue is dominant, the electronic density is locally concentrated at each atomic basin and the interaction is classified as closed shell which is typical of highly ionic bonds, hydrogen bonds, and van der Waals interactions. This particular interaction is described by relatively low $\rho(r)$ values, $\nabla^2\rho(r) > 0$ and $\lambda_1/\lambda_3 < 1$; $\rho(r)$ is contracted from the interatomic surface by accumulating in the individual atomic basins of the interacting atoms, and it can be said that the electrons are delocalized with respect to the bond path. The interaction between the metal and the remaining atoms of the coordination sphere has a non-covalent nature that is “ionic nature”. Furthermore, the presence of neat electron charges both on the transition metal and the atomic species surrounding it suggests that the bonding within the coordination sphere is ionic in nature (see Table S4). The values of $\rho(r)$ and $\nabla^2\rho(r)$for the Cu-ligand interactions are in good agreement with the earlier theoretical results for Mn^{2+}, Co^{2+}, Ni^{2+}, Cu^{2+} and Zn^{2+} complexes (~0.03–0.07 a.u.) [28,32]. In this case, the electronic density values are higher than those in the early report, which would indicate higher structural stability.

Comparing the data appearing in Table 3, it can be observed that the values of the electronic density $\rho(r)$ at the BCPs for the main interactions are at least twice or three times higher than those for the weakest contributions. The values of the electron density obtained for hydrogen bonding interactions fall within a range of 0.0320–0.0155 a.u. and their Laplacian values are positive (0.114–0.074 a.u.), indicating closed shell interactions. High electron density values are associated with the Cu––O(30) and O(33)–H––O(16) interactions.

3.7. NBO analysis

The role of hyperconjugative interactions in the stabilization of the complex has been assessed using NBO analysis, where the hyperconjugation represents the transfer of an electron between a lone pair or bonding orbital and an antibonding orbital [31,32]. The main hyperconjugative interactions for the [Cu(uracilato-N^1)$_2$(NH_3)$_2$] ·2H_2O are shown in Table 4. As shown in Table 4, the donor natural orbitals correspond to lone pairs of the atoms linked

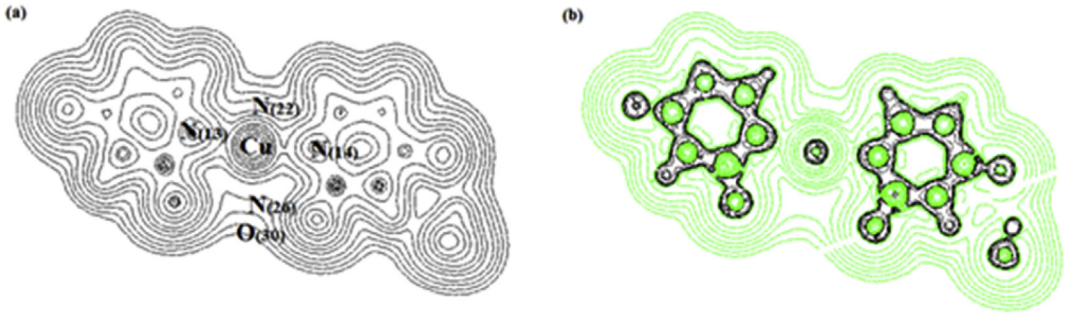

Fig. 12. (a) Topological surface of the density contour map for the complex; (b) Contour map of the Laplacian for the complex in the plane containing the atoms of the coordinating sphere. The atoms that lie in the plane of the figure are indicated by circles. Dotted/continuous lines correspond to positive/negative values of $\nabla^2 \rho$ (r); where the electronic density is decreased/concentrated.

Table 3
Topological properties of the electron density at the bond critical point (BCP) for the [Cu(uracilato-N^1)$_2$ (NH_3)$_2$]·2H_2O complex (in a.u.).

Bond (X–Y)	ρ(r)	$\nabla^2\rho$ (r)	λ_1/λ_3
Cu–N(13)	0.0765	0.420	0.165
Cu–N(14)	0.0767	0.420	0.166
Cu–N(22)	0.0635	0.360	0.153
Cu–N(26)	0.0708	0.380	0.160
Cu–O(30)	0.0323	0.160	0.147
N(26)-H—O(15/17)	0.0192	0.078	0.194
N(22)-H—O(30)	0.0155	0.074	0.183
O(30)–H–-O(15/17)	0.0282	0.104	0.225
O(33)–H–-O(16)	0.0320	0.114	0.235

to the transition metal, LP N→LP* Cu. Our results reveal an important contribution to the stabilization of the coordination sphere due to the hyperconjugative interaction LP O(30)→LP* Cu involving the lone pair of the oxygen atom and the metal center. It is important to emphasize the strength of the hydrogen bond of the second hydration water attached to one of the uracil rings with a similar value to the Cu–O bond. Anyway, taking into account the positive values of the Laplacian on the BCPs for the metal–ligand bonds, we consider that the NBO results overestimate the covalent character of these bonds. These results are in agreement with the data previously reported for Illán-Cabeza et al. [31] for various metal complexes.

Table 4
Important hyperconjugative interactions for [Cu(uracilato-N^1)$_2$ (NH_3)$_2$]·2H_2O.

Donor → Acceptor[a]	ΔE/kJ mol^{-1}
σ C(3)–N(13) →LP* Cu	3.24
σ C(8)–N(14) →LP* Cu	3.52
σ C(9)–N(14)→LP* Cu	3.26
LP N(13)→LP* Cu	39.50
LP N(14)→LP* Cu	39.85
LP N(22)→LP* Cu	34.18
LP N(26)→LP* Cu	37.12
LP O(30)→LP* Cu	20.23
LP(1) O(30)→LP* N(22)–H	2.60
LP(2) O(30)→LP* N(22)–H	2.01
LP(1) O(15/17)→LP* N(26)–H	1.60
LP(2) O(15/17)→LP* N(26)–H	3.60
LP(1) O(15/17)→LP* O(30)–H	6.98
LP(2) O(15/17)→LP* O(30)–H	11.70
LP(1) O(16)→LP* O(33)–H	8.03
LP(2) O(16)→LP* O(33)–H	21.27

[a] LP is a lone pair on the specified atom (see Fig. 1 for atom numbering).

4. Conclusions

The metal complex [Cu(uracilato-N^1)$_2$(NH_3)$_2$]·2H_2O was synthesized and characterized by different spectroscopic techniques. The geometrical parameters obtained by quantum chemical calculations were compared with the experimental ones obtained by XRD data previously reported showing a good agreement between them. From the X-ray structure of the complex we were able to determinate that the intermolecular O···H contacts have the major contribution to the crystal packing (43.5%) and the H···H contacts comprise 33.4% of total Hirshfeld surface area of the complex. Other types of intermolecular contacts with the most important percentages occur such as C···H (13.1%), N···H (3.3%), C···N (1.5%) and C···C (1.2%). The supramolecular assembly of the complex was also characterized by π-stacking interactions between the uracil rings. Shape index and curvedness were useful to visualize and analyze π-stacking in both sides of the molecule.

A complete assignment of the IR and Raman wavenumbers of the metal complex in solid state was made, with some corrections in the previous assignment of the uracil ligand.

The results of TG-DT analysis indicates that the complex chemically decomposes through a one step reaction with a mass loss consistent to the formation of CuO as final product.TD-DFT investigation gave insights into the optical transitions involved in the excitation process. From our theoretical results, all of the low-lying electronic states were characterized as a mixture of ILCT and LMCT transitions.

From the AIM and NBO analysis we concluded that the interactions from the LP of the nitrogen atoms of the ligands to the antibonding d orbitals of Cu are much stronger than those of the free metal pairs towards the ligands; besides the π-donors are stronger than the σ-donors. A deeper insight into the nature and strength of the electron transfer process in the complex can be achieved by studying of electronic densities near the active donor and acceptor sites. It was found that the N atom functions as an electron donation center, while the Cu atom is classified as the most electron acceptor. This fact is reflected in the UV–visible spectrum where the band at 276 nm is related to the ligand-to-metal charge transfer (LMCT).

Despite much progress accomplished in the area of metal-ligand interactions to achieve a better understanding of the role of metal ions in biological systems, this work represents a deeper insight into the interaction of the uracil ligand with the Cu^{2+} metal ion from both an experimental and a theoretical point of view.

Acknowledgements

This work was supported by SCAIT (D542/2), CONICET (PIP

0205) and ANPCyT (PICT0697).

The authors thank to Junta de Andalucía, Spain (FQM-337) and "Centro de Servicios de Informática y Redes de Comunicaciones" (CSIRC)(2), Universidad de Granada (Spain)(1) for providing the computing time.

Supporting information available:

Experimental and calculated geometric parameters for bis(uracilato)diammine Cu (II) complex (Table S1); Bis(uracilato)diammine Cu (II) complex hydrogen bond distances in the solid state and calculated ones (Table S2); Selected bands calculated and observed in the Infrared and Raman spectra of bis(uracilato)diammine Cu (II) complex(Table S3); AIM and NBO atomic charge (a.u.) for [Cu(uracilato-N^1)$_2$ (NH_3)$_2$] ·2H_2O theoretical optimized geometries (Table S4); Important Hyperconjugative Interactions for [Cu(uracilato-N^1)$_2$ (NH_3)$_2$] ·2H_2O (Table S5); A view of the hydrogen bonding interactions for the complex [Cu(uracilato-N^1)$_2$(NH_3)$_2$]·2H_2O(Fig. S1).

Appendix A. Supplementary data

Supplementary data related to this article can be found at https://doi.org/10.1016/j.molstruc.2017.11.030.

References

[1] E. Freisinger, R.K.O. Sigel, From nucleotides to ribozymes—a comparison of their metal ion binding properties, Coord. Chem. Rev. 251 (2007) 1834.
[2] A. Terrón, J.J. Fiol, A. García-Raso, M. Barceló-Oliver, V. Moreno, Biological recognition patterns implicated by the formation and stability of ternary metal ion complexes of low-molecular-weight formed with amino acid/peptides and nucleobases/nucleosides, Coord. Chem. Rev. 251 (2007) 1973.
[3] M. Goodgame, K.W. Johns, Metal complexes of uracil and thymine, J. Chem. Soc. Dalton Trans. (1977) 1680–1683.
[4] J.R.J. Sorenson, in: H. Sigel, M. Dekker (Eds.), Metal ions in biological systems, 14, 1982, pp. 77–124. New York.
[5] C.C. Wagner, E.J. Baran, Vibrational Spectra of Bis(L-Methioninato)Copper(II), Acta Farmacéutica Bonaerense 21 (2002) 287–290.
[6] A. Terrón, A. García-Raso, J.J. Fiol, S. Amengual, M. Barceló-Oliver, R.M. Tótaro, M.C. Apella, E. Molins, I. Mata, Uracilato and 5-halouracilato complexes of Cu(II), Zn(II) and Ni(II). X-ray structures of [Cu(uracilato-N(1))(2)(NH(3))(2)].2(H(2)O), [Cu(5-chlorouracilato-N(1))(2)(NH(3))(2)](H(2)O)(2), [Ni(5-chlorouracilato-N(1))(2)(en)(2)].2H(2)O and [Zn(5-chlorouracilato-N(1))(NH(3))(3)]. (5-chlorouracilato-N(1)). (H(2)O), J. Inorg. Biochem. 98 (2004) 632–638.
[7] J.P. Henderson, J. Byun, J. Takeshita, J.W. Heinecke, Phagocytes produce 5-chlorouracil and 5-bromouracil, two mutagenic products of myeloperoxidase, in human inflammatory tissue, J. Biol. Chem. 278 (2003) 23522–23528.
[8] A. García-Raso, J.J. Fiol, B. Adrover, P. Tauler, A. Pons, I. Mata, E. Espinosa, E. Molins, Reactivity of copper (II) peptide complexes with bioligands (benzimidazole and creatinine), Polyhedron 22 (2003) 3255–3264.
[9] B. Lippert, Multiplicity of metal ion binding patterns to nucleobases, Coord. Chem. Rev. 200–202 (2000) 487–516.
[10] R.F.W. Bader, Atoms in and Molecules. A Quantum Theory, Clarendon Press, Oxford, 1990.
[11] a) P.J. Hay, W.R. Wadt, *Ab initio* effective core potentials for molecular calculations. Potentials for the transition metal atoms Sc to Hg, J. Chem. Phys. 270 (1985) 270;
b) P.J. Hay, W.R. Wadt, *Ab initio* effective core potentials for molecular calculations. Potentials for main group elements Na to Bi, J. Chem. Phys. 82 (1985) 284;
c) P.J. Hay, W.R. Wadt, Ab initio effective core potentials for molecular calculations. Potentials for K to Au including the outermost core orbitals, J. Chem. Phys. 82 (1985) 299.
[12] A.D. McLean, G.S. Chandler, Contracted Gaussian basis sets for molecular calculations. I. Second row atoms, Z=11-18, J. Chem. Phys. 72 (1980) 5639–5648.
[13] R. Krishnan, J.S. Binkley, R. Seeger, J.A. Pople, Self-consistent molecular orbital methods. XX. A basis set for correlated wave functions, J. Chem. Phys. 72 (1980) 650–654.
[14] E.D. Glendening, J.K. Badenhoop, A.E. Reed, J.E. Carpenter, F.F. Weinhold, NBO 3.1 Theoretical Chemistry Institute, University of Wisconsin, Madison, WI, 1996.
[15] J.P. Foster, F. Weinhold, Natural hybrid orbitals, J. Am. Chem. Soc. 102 (1980) 7211–7218.
[16] A.E. Reed, R.B. Weinstock, F. Weinhold, Natural-population analysis, J. Chem. Phys. 83 (1985) 735–746.
[17] M.J. Frisch, et al., Gaussian 09, Revision B.01, Gaussian, Inc., Wallingford, CT, USA, 2009.
[18] F. Biegler-König, J. Schönbohm, AIM 2000 Version 2.0, University of Applied Science, Bielefeld, Germany, 2002.
[19] B. Nielsen, A.J. Holder, GaussView, User's Reference; GAUSSIAN Inc.: Pittsburgh, PA, 1997–1998.
[20] C.V. Caillie, R.D. Amos, Geometric derivatives of excitation energies using SCF and DFT, Chem. Phys. Lett. 308 (1999) 249–255.
[21] R.E. Stratmann, G.E. Scuseira, M.-J. Frisch, An efficient implementation of time-dependent density-functional theory for the calculation of excitation energies of large molecules, J. Chem. Phys. 109 (1998) 8218–8224.
[22] M.A. Spackman, D. Jyatilaka, Hirshfeld surface analysis, Cryst. Eng. Comm. 11 (2009) 19–32.
[23] M.A. Spackman, J.J. McKinnon, Fingerprinting intermolecular interactions in molecular crystals, Cryst. Eng. Comm. 4 (2002) 378–392.
[24] J.J. McKinnon, M.A. Spackman, A.S. Mitchel, Novel tools for visualizing and exploring intermolecular interactions in molecular crystals, Acta Cryst. B 60 (2004) 627–668.
[25] J.J. McKinnon, D. Jayatilaka, M.A. Spackman, Towards quantitative analysis of intermolecular interactions with Hirshfeld surfaces, Chem. Commun. (2007) 3814–3816.
[26] M. Graindourze, T. Grootaers, J. Smets, Th Zeegers-Huyskens, G. Maes, FT-IR spectroscopic study of uracil derivatives and their hydrogen bonded complexes with proton donors: II. Monomer IR absorptions of thiouracils and 5-halogeno-uracils in argon matrices, J. Mol. Struct. 237 (1990) 389–410.
[27] Z. Wang, F. Zhang, X. Zeng, H. Zhou, B. Gu, W. Cheng, Vibrational properties of uracil, Chin. Sci. Bull. 51 (2006) 1804–1810.
[28] M.R. Viant, R.S. Fellers, R.P. McLaughlin, R.J. Saykally, Infrared laser spectroscopy of uracil in a pulsed slit jet, J. Chem. Phys. 103 (1995) 9502–9505.
[29] U. Koch, P.L.A. Popelier, Characterization of C-H-O hydrogen bonds on the basis of the charge density, J. Phys. Chem. 99 (1995) 9747–9754.
[30] S. Kavitha, P. Deepa, M. Karthika, R. Kanakaraju, Topological analysis of metal–ligand and hydrogen bonds in transition metal hybrid structures – A computational study, Polyhedron 115 (2016) 193–203.
[31] N.A. Illán-Cabeza, S.B. Jiménez-Pulido, F. Hueso-Ureña, T. Peña-Ruiz, M. Quirós-Olozábal, M.N. Moreno-Carretero, Interactions between 2,4-bis-pteridine-1,5-benzodiazepine and group 12 dihalides: synthesis, spectral and XRD structural studies and theoretical calculations, Dalton Trans. 45 (2016) 17896–17909.
[32] Frenking, N. Fröhlich, The nature of the bonding in transition-metal compounds, Chem. Rev. 100 (2000) 717–774.